Appendix C:
Software

The complete analysis of the data associated with the CE-06 experiment required the development of specialized software for both VMS® and UNIX® platforms. Most of this software is directly related to describing the passage of charged particles through the T-Site 6° magnet and the CE-06 detection apparatus. This appendix discusses the key elements of the software and corresponding use in the analysis of the experimental data.

C.1   The T-Site Magnet Map

Central to the software discussed here is the magnetic field map of the six-degree T-Site dipole. The large-gap design of the magnet, while permitting extremely efficient detection of recoils, results in a fringe field of considerable extent, as seen in Figs. 3.8 and 3.11. As such, a three-dimensional map of **B** is necessary in order to realistically integrate the equations of motion for charged particles traversing the magnetic field.

Analytical calculations of the magnetic field (the results of which are referred to hereafter as the "TOSCA" map) using the expected magnet pole design parameters were completed [Dk91] before the magnet was actually built, to test its suitability to the ring. The fixed coordinate system ("magnet" coordinates) used throughout this work was chosen to match as closely as possible that used in the TOSCA code, for convenience of comparison. The origin of this system is located vertically midway between the magnet pole faces and horizontally in the middle of the B_y field plateau (see Fig. 3.6). Defined to be parallel to the magnet mapper axes, the x and z axes lie in a plane parallel to the pole faces. The y-axis is perpendicular to the poles, with $y = 0$ symmetrically located halfway between. In this manner, the nominal beam direction is along the z-axis, although particular particle trajectories encountered during the ring cycle may yield incident angles on the order of 0.2° to this axis.

The IUCF magnet mapper measured the y-component of the magnetic field in xz-

plane grids at several values of y, including $y = 0$. Since standard ring dipole magnets are typically mapped only in the bend plane, it was necessary to translate the $6°$ magnet along the y-axis for each desired xz-plane grid. In order to construct the complete map using this data, calculations were performed as follows. First, the data was interpolated to generate a uniformly spaced grid of B_y values in three dimensions. This was necessary since the measured grids were not uniformly spaced over their extents, and the grids of some planes were shifted and rotated with respect to the grid at $y = 0$. The corrections for the latter effects were determined from the measured coordinates of three fiducial marks (essentially, pins in the pole faces) taken during each grid measurement.

Next, the B_x and B_z components of the field were calculated at each (x, y, z) grid vertex, in the following way. From symmetry about the $y = 0$ plane,

$$B_{x,z} \approx y\frac{\partial B_{x,z}}{\partial y} + \frac{y^3}{3!}\frac{\partial^3 B_{x,z}}{\partial y^3}$$

and

$$B_y \approx B_y(y = 0) + \frac{y^2}{2!}\frac{\partial^2 B_y}{\partial y^2} + \frac{y^4}{4!}\frac{\partial^4 B_y}{\partial y^4}.$$

Using

$$\boldsymbol{\nabla} \times \mathbf{B} = 0 = \boldsymbol{\nabla} \cdot \mathbf{B},$$

the partial derivatives of B_x and B_z can be expressed in terms of derivatives of B_y. With

$$B_{x,z}(x, y, z) = -B_{x,z}(x, -y, z)$$

and

$$B_y(x, y, z) = +B_y(x, -y, z),$$

the components can be written

$$B_x = \frac{y}{2\Delta}\Big(B_y(x + \Delta, 0, z) - B_y(x - \Delta, 0, z)\Big)$$
$$+ \frac{y^3}{24\Delta^3}\Big(B_y(x + \Delta, 2\Delta, z) - B_y(x + \Delta, 0, z)$$
$$+ B_y(x - \Delta, 0, z) - B_y(x - \Delta, 2\Delta, z)\Big),$$

$$B_z = \frac{y}{2\Delta}\Big(B_y(x, 0, z + \Delta) - B_y(x, 0, z - \Delta)\Big)$$
$$+ \frac{y^3}{24\Delta^3}\Big(B_y(x, 2\Delta, z + \Delta) - B_y(x, 0, z + \Delta)$$
$$+ B_y(x, 0, z - \Delta) - B_y(x, 2\Delta, z - \Delta)\Big),$$

and

$$B_y = B_y(y = 0) + \frac{y^2}{4\Delta^2}\Big(B_y(x, 2\Delta, z) - B_y(x, 0, z)\Big)$$
$$+ \frac{y^4}{192\Delta^4}\Big(B_y(x, 4\Delta, z) - 4B_y(x, 2\Delta, z) + 3B_y(x, 0, z)\Big).$$

Here, Δ is the grid size, which for the T-Site map is 1 cm. These equations allow the complete calculation of the magnetic field map.
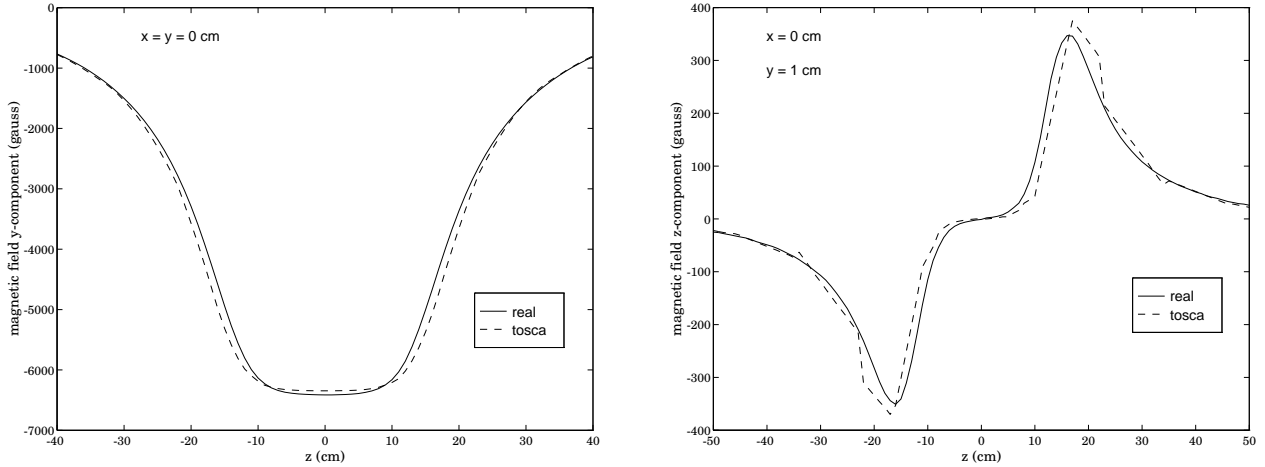

Figure C.1   The B_y (left) and B_z (right) components of the real (solid line) and TOSCA (dashed line) field maps as a function of z. Both fields are for a magnet current of 300 amps.

The strength and shape of this "real" field agree well with that calculated using the TOSCA code. Figure C.1 shows a representative comparison. As a final step in the construction of the map, those regions of space around the magnet for which B_y data could not be obtained (due to physical or temporal constraints) were "filled in" with the TOSCA field. Most particles entering this region (see Fig. C.2) fail to enter the detector stack because either they are too "soft" or they hit the aluminum pole-face spacer. However, raytracing calculations showed that transporting particles through the non-mapped region and assuming $B = 0$ here could result in false simulation of events in the CE-06 detectors. Use of the TOSCA field obviated the need for any time-consuming dipole field approximations in this region.

C.2   Forward Raytracing Simulations

Simulation software was developed for the CE-06 experiment primarily to determine the experimental acceptance as a function of the charge state, momentum, and reaction
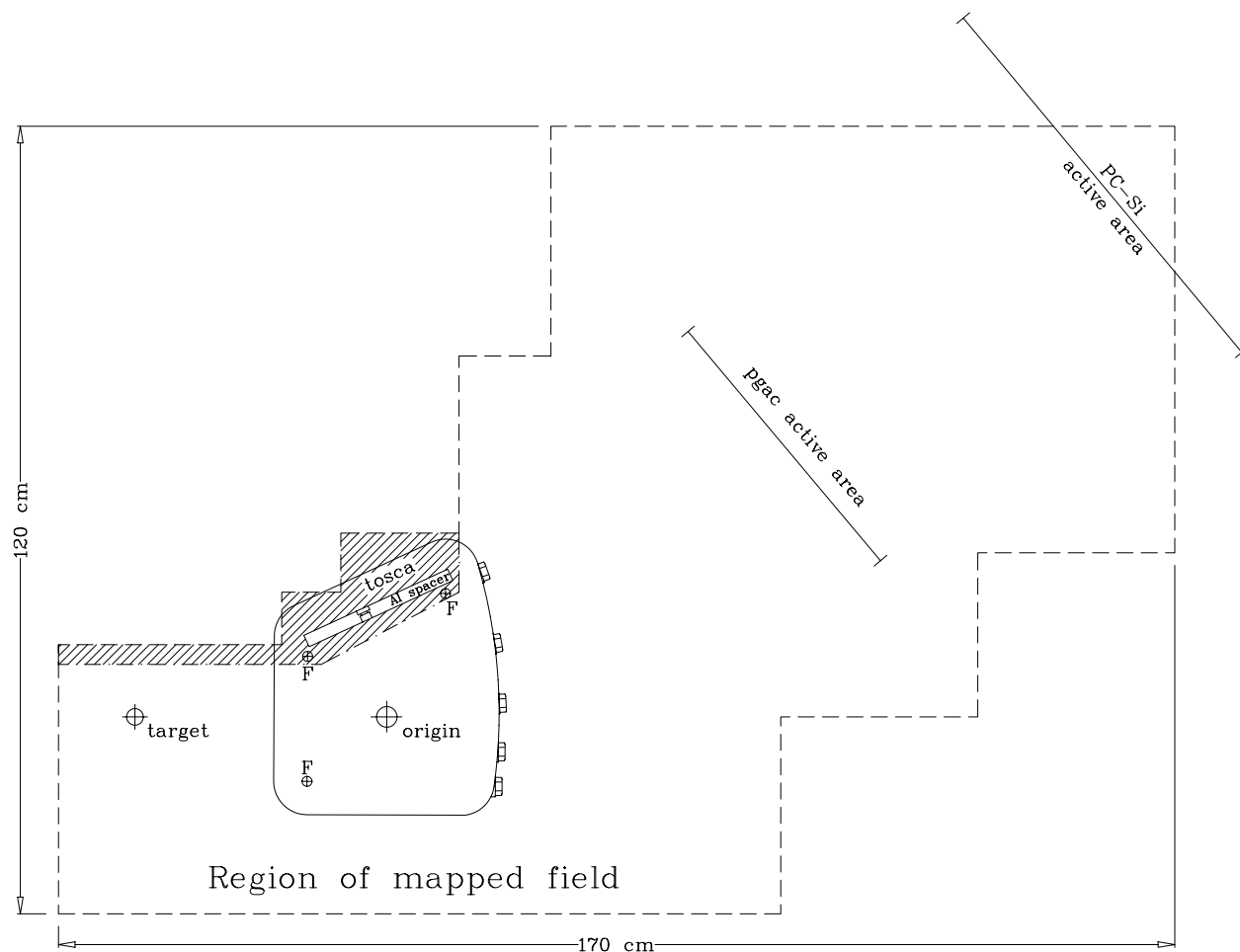
Figure C.2   Extent of the measured (white area) and TOSCA (hatched area) portions of the final map, with the locations of the PGAC and PC-Si for reference. Also shown are the locations of the fiducial pins ("F"), used for the absolute position calibration, and the aluminum spacer placed between the pole faces to assure a constant pole separation.

angle of recoil ions. The software was also used to estimate the effects of energy loss, charge redistribution, and multiple scattering of the ions in the pressure foils. Several specialized programs (e.g., for extraction of acceptance functions or simulation of online histograms) were written to utilize a core program for "forward" raytracing of ions through the magnet map of Sec. C.1. This core program transports ions from the target location, through the magnetic field, and into the detector stack, keeping track of the particle's magnet coordinates, energy losses, and velocity direction changes due to multiple scattering.

The most important element of the program is the magnetic transport of the charged particles. Here, a simple second-order midpoint method is used to integrate the equations of motion. A comparison with a fourth-order Runge-Kutta method [Pr88] showed negligible

track differences, and so the second-order method was chosen to improve execution speed. Far from the detector planes, an integration step size on the order of the grid size Δ is used. Within distance Δ of a detector's active area, however, the step size is reduced typically by a factor of five, for accurate position determination at the plane. This position is determined by an interpolation to the intercept point using the ion track's step coordinates before and after the detector plane. At each step, the magnetic field value is determined via three-dimensional quadratic interpolation of the grid.

Less complicated (but nonetheless important) elements of the forward raytracing include the simulation of energy losses and multiple scattering, both of which are especially relevant for heavily ionizing particles. Energy losses are calculated at each interception of the ion with material. The energy loss is assumed to take place at a point in space for foils, while for extended matter such as gas the losses are averaged over the ion's track in the material. Reasonably accurate (estimated error of 15% or better) energy loss numbers were obtained through the use of data tables [No70] from which $\Delta E(E, Z, M)$ for each type of material could be determined. Table C.1 shows estimates of the data analysis parameters of Ch. 4 for recoils from pion-production reactions at $E_p = 330$ MeV, obtained using the forward raytracing and energy loss tables.

	$^{12}C(p,\pi^+)^{13}C_{g.s.}$			$^{12}C(p,\pi^0)^{13}N_{g.s.}$		
	$p = p_{\min}$	$\theta = \theta_{\max}$	$p = p_{\max}$	$p = p_{\min}$	$\theta = \theta_{\max}$	$p = p_{\max}$
E_{reac} (MeV)	13.17	25.62	49.89	13.15	25.62	49.94
E_{tof} (MeV)	10.0	23.4	48.4	9.0	22.7	48.0
E_{si} (MeV)	7.0	21.5	47.2	5.0	20.1	46.3
ΔE (MeV)	0.7	0.4	0.3	0.9	0.6	0.4
R_{m} (mg/cm^2)	1.9	4.1	10.4	1.5	3.2	8.0

Table C.1   Characteristic energy values and ranges in mylar, calculated using forward raytracing, for ^{13}C and ^{13}N recoils. The reaction energies E_{reac} correspond to $p_{\min}$, $p(\theta_{\max})$, and $p_{\max}$ of the $E_p = 330$ MeV recoil locus.

Multiple scattering is incorporated in the raytracing code via the improved [Hi75] Highland formula: given the momentum p and velocity β of an ion with atomic number Z_{ion}, the r.m.s. scattering angle with respect to the incident direction is

$$\frac{\theta_{\text{rms}}}{\sqrt{2}} = \frac{13.6 \text{ MeV}}{\beta pc} Z_{\text{ion}} \sqrt{\frac{L}{L_{\text{mat}}}} \left[1 + 0.088 \cdot \log_{10} \left(\frac{L}{L_{\text{mat}}} \cdot \frac{Z_{\text{ion}}^2}{\beta^2} \right) \right], \qquad \text{(C.1)}$$

where L_{mat} is the scattering material's radiation length, and L is the scatterer's thickness. The scattering is calculated at each traversal by the ion of a pressure foil in the CE-06 setup[1] by generating a random angle with the proper distribution and r.m.s. value given by Eq. (C.1). Although fairly accurate (10%) for material thicknesses in the range $10^{-3} < L/L_{mat} < 100$, the uncertainty in θ_{rms} for the CE-06 thin foil thicknesses of $L/L_{mat} \approx 3.5 \times 10^{-6}$ is not known. Nonetheless, it is important and necessary to include the effects of multiple scattering in the analysis of the CE-06 data (see Chapter 4).

A complete simulation of the experiment is possible as a shell using this forward ray-tracing kernel. A reaction event ion at the target is generated with a given center-of-mass angular distribution, which may be isotropic or an arbitrary combination of Legendre polynomials to simulate a realistic cross-section. With an atomic charge Q, chosen according to the appropriate energy dependence as in Fig. 3.10, the forward raytracing is called and the resulting information (such as time-of-flight, silicon position, etc.) is histogrammed. In this way, the effects of energy loss, multiple scattering, and acceptance on the apparent angular distribution with respect to the center-of-mass cross-section can be separately investigated. Furthermore, the performance of the backward raytracing code as used in the analysis can be examined.

C.3 Backward Raytracing

Given a recoil ion's detector signatures (deposited energies, measured positions, and so forth), it is necessary to completely reconstruct the ion's reaction parameters; this is the thrust of the analysis in Ch. 4. A major part of this reconstruction is the determination of the recoil's momentum and emission angle at the (known) target location, using the position and angle of the ion at the exit of the magnet box. In principle, this could be accomplished by "backward" raytracing, i.e., magnetic transport identical to Sec. C.2 except with $t \mapsto -t$. If the mass and reaction energy of the ion were known, then, by requiring that the recoil come from the target location, the emission angle (and, as a by-product, the atomic charge Q) would be determined.

In the analysis of the CE-06 data, however, uncertainties in the determination of the mass made it impossible to completely identify M without using more information, specifically, the ion's rigidity $R \equiv p/Q$. Furthermore, the calculation of the reaction energy of the ion (using the measured value of energy at the silicon detectors as a starting

---

[1] The contribution of multiple scattering in the gases is negligible in comparison.

point) was limited to about 10% accuracy. This uncertainty was primarily due to the (unmeasured) energy losses in the intervening foils and gases, and, to a lesser extent, systematic errors in the thicknesses of the materials themselves. True backward raytracing was therefore of limited use, and so a code was developed which could determine rigidity and angle at the target while avoiding the need to estimate these unknown quantities.

This backward raytracing program[2] depends on the fact that a PGAC-Si position pair can be uniquely associated with a R-θ_p pair (where θ_p is the bend-plane angle of the ion, not the spherical angle θ, cf. Fig. 4.17), for a wide range of ion masses, energies, and nuclear charges. For an arbitrary magnetic field, however, the function which connects these pairs cannot be determined analytically. Therefore, the forward raytracing was implemented to generate a set of ion tracks for kinematically possible momenta and angles, using reactions of particular interest[3] to the experiment, for each beam energy desired. In general, due to the small vertical acceptance[4] of the detector stack, it was only necessary here to use ion trajectories in the x-z plane.

Using this data, fits were made in an attempt to determine polynomial functions which could reproduce the initial rigidity and angle pairs with errors no worse than 1% and 0.1°, respectively, with a "reasonable" number of parameters. The best results were obtained with

$$\theta_p(x_{\mathrm{pg}}, x_{\mathrm{si}}) = a_0 + a_1 x_{\mathrm{pg}} + a_2 x_{\mathrm{si}}$$
$$+ a_3 x_{\mathrm{pg}} x_{\mathrm{si}} + a_4 x_{\mathrm{pg}}^2 + a_5 x_{\mathrm{si}}^2$$
$$+ a_6 x_{\mathrm{pg}} x_{\mathrm{si}}^2 + a_7 x_{\mathrm{pg}}^2 x_{\mathrm{si}} + a_8 x_{\mathrm{pg}}^3 + a_9 x_{\mathrm{si}}^3 \; ;$$

$$R(x_{\mathrm{pg}}, x_{\mathrm{si}}, \theta_p) = b_0 + b_1 \theta_p + b_2 \theta_p^2 \qquad\qquad \text{(C.2)}$$
$$+ (b_3 + b_4 \theta_p) x_{\mathrm{pg}} + (b_5 + b_6 \theta_p) x_{\mathrm{si}}$$
$$+ b_7 x_{\mathrm{si}}^2 \theta_p + b_8 x_{\mathrm{pg}}^2 \theta_p + (b_9 + b_{10} \theta_p) x_{\mathrm{pg}} x_{\mathrm{si}}$$
$$+ (b_{11} + b_{12} \theta_p)/x_{\mathrm{si}} + (b_{13} + b_{14} \theta_p)/x_{\mathrm{pg}}.$$

Here, x_{pg} and x_{si} are the ion positions along the length of the active areas of the PGAC and Si detectors, respectively (cf. Fig. 4.2). Standard least-squares minimization techniques were used to determine the coefficient vectors **a** and **b**. A set of parameters was calculated for tracks incident upon each half of the PGAC, to constrain the range of fitted values for

---

[2] Technically, a misnomer, since no real-time raytracing is done.

[3] The traced ions consisted primarily of ^{13}C and ^{13}N.

[4] The vertical angular width presented to the target by the silicon array is roughly 2°.

R and θ_p.

The forward raytracing which provides the input data for these fits includes the phys-ical detector data, specifically, the locations of the PGAC and Si active areas with respect to the magnetic field, as determined in the calibration procedures of Ch. 4. Therefore, it is not necessary to determine the explicit form of the transformation (4.4); this is already incorporated in Eq. (C.2). In the absence of an analytical function, the fit provides an efficient means to combine the raytracing and transformation calculations into a routine suitable for on-line data analysis (i.e., without CPU-intensive code).
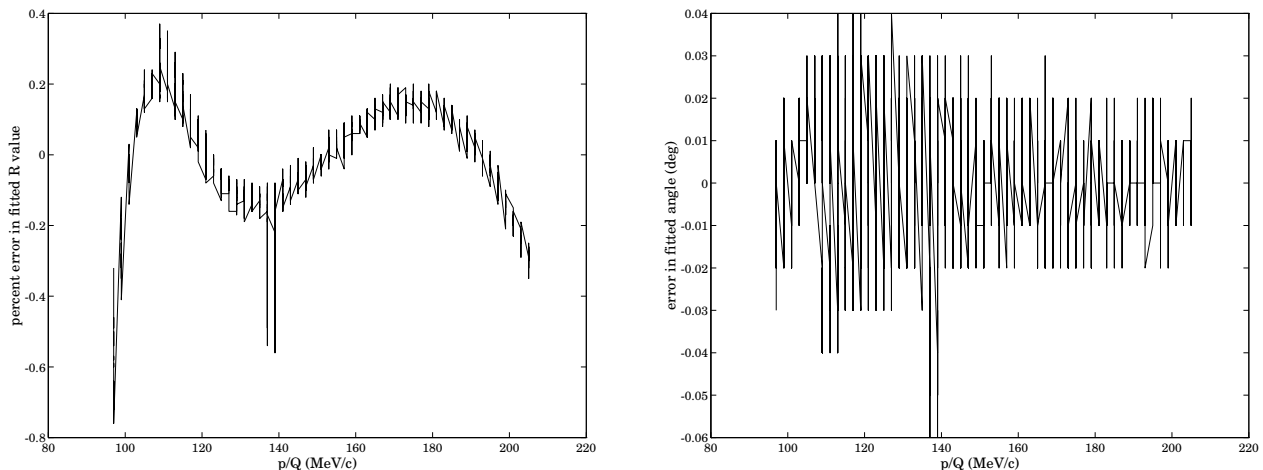

Figure C.3   Errors in a typical fit to forward raytracing data for $E_p = 294$ MeV, using Eq. (C.2). Shown are $\delta R/R \times 100$ (left) and $\delta\theta_p$ (right), for each point in the input data. The maximum errors in absolute value for this case are 0.8% and 0.06° for the rigidity and angle fits, respectively.

Use of the calculated angle in the rigidity function not only helps to constrain this fit, resulting in a simpler functional form, but also serves to eliminate ambiguities that would surface using independent functions. These ambiguities arise due to the finite resolution of the PGAC and Si position measurements. For example, it is possible for two ions to be emitted with rigidities that differ by more than 1%, but which produce the same x_{pg} and x_{si} values within the respective detector resolutions. In this case, the angle is necessary to distinguish the two values of rigidity.

The quality of the fits that can be achieved is good: particular results for $E_p = 294$ MeV are shown in Fig. C.3. In general, the average difference errors between the fit and the input data for this functional form were typically 0.2% for rigidity and 0.01° for angle, although errors for very soft ions ($p/Q < 90$ MeV/c) often ranged from 1–2%. In these cases the curvature of the ion track is large and so the momentum is very sensitive

to the detector positions. For the CE-06 experiment, however, most of the ions of interest were not in this range of rigidity.

As an independent test, the backward raytracing was used with α-particle source data (using a target-mounted ^{228}Th source), for which the mass, energy, and atomic charge of the ions were known *a priori*. In this manner, the goodness of the fit in determining R-θ_p pairs for data not explicitly in the forward raytracing input sets could be ascertained. After the calibration corrections of Ch. 4, the rigidities obtained for the four α-particle lines (103 MeV/c $\leq R \leq$ 128 MeV/c) used in Fig. 4.5 matched the tabulated values to within 0.4%. These results suggested that the fits were applicable to all the data of the CE-06 experiment, with characteristic errors given by Fig. C.3.